3D Printed Silicone Meniscus Implants

Subjects: Polymer Science

Contributor: Houwen Matthew Pan, Eric Luis, Anil K. Bastola, Ram Bajpai, Swee Leong Sing, Wai Yee Yeong

Osteoarthritis of the knee with meniscal pathologies is a severe meniscal pathology suffered by the aging population worldwide. However, conventional meniscal substitutes are not 3D-printable and lack the customizability of 3D printed implants and are not mechanically robust enough for human implantation. Similarly, 3D printed hydrogel scaffolds suffer from drawbacks of being mechanically weak and as a result patients are unable to execute immediate post-surgical weight-bearing ambulation and rehabilitation. To solve this problem, we have developed a 3D silicone meniscus implant which is (1) cytocompatible, (2) resistant to cyclic loading and mechanically similar to native meniscus, and (3) directly 3D printable. The main focus of this study is to determine whether the purity, composition, structure, dimensions and mechanical properties of silicone implants are affected by the use of a custom-made in-house 3D-printer. We have used the phosphate buffer saline (PBS) absorption test, Fourier transform infrared (FTIR) spectroscopy, surface profilometry, thermo-gravimetric analysis (TGA), X-ray photoelectron spectroscopy (XPS), differential scanning calorimetry (DSC), and scanning electron microscopy (SEM) to effectively assess and compare material properties between molded and 3D printed silicone samples.

Keywords: additive manufacturing ; 3D printing ; silicone ; meniscus implants ; validation

1. Introduction

Ten percent of the entire global population are elderly over the age of 65 suffering from osteoarthritis of the knee with meniscal pathologies [1][2]. More than one million cases of knee surgeries are performed annually in the US alone. However, current total meniscal substitute like NUSurface meniscal implant [3], which are currently undergoing Food and Drug Administration (FDA) Phase 2 Sun Clinical Trials, are not 3D printed and are not customizable. CMI [4] and Actifit [5] [6] are the two natural and synthetic porous meniscal implants, respectively, used for symptomatic post-meniscectomy patients, provided that there are residual peripheral meniscus and minimal cartilage damage. They also suffer from the drawback of being weak mechanically and are approved for used in chronic meniscal injuries only.

The utilization of additive manufacturing technologies to develop highly customizable and application-oriented prototypes or mechanical parts have gained popularity in the past two decades [7]. More recently, even functional prototypes and end products have been made printable as the cost of 3D printers and inks became more affordable and more sophisticated softwares were developed [8]. However, current 3D printed scaffolds, using polyvinyl alcohol (PVA) or hydrogels [8][9][10], are mechanically weak and as a result patients are not able to execute immediate post-surgical weight-bearing ambulation and rehabilitation.

Liquid silicone rubbers (LSR) are silicone rubbers with additional vulcanization, and widely used in medical, construction, automotive, electronics, and the food industry, due to their excellent thermal and biocompatibility properties, low viscosity, controllable crosslinking and easy implementation. LSR are cross-linked by a hydrosilylation mechanism, which refers to the addition of Si–H bonds to carbon double bonds borne by poly(dimethylsiloxane) chains. LSR formulations are mainly composed of unsaturated silicone rubber (component A), polysiloxane has silane (Si–H) functional groups (component B) and platinum compound catalyst such as Karstedt's catalyst [11]. The hydrosilylation reaction of LSR is presented in Figure 1.

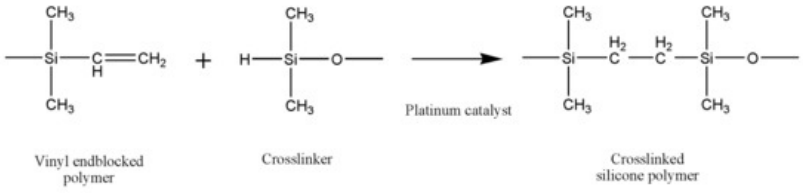

Figure 1. The hydrosilylation reaction of liquid silicone rubbers.

A number of different types of 3D printing techniques have been used to 3D print the silicone elastomers and their composites, such as direct ink writing (DIW) 3D printing [12][13][14][15][16][17], digital light synthesis (DLS) 3D printing [18][19], inkjet 3D printing [20], drop-on-demand [21][22] and even modified fused deposition modeling (FDM) 3D printing [7][23][24]. The silicone elastomers and their composites are potential candidate materials in a number of different applications including soft sensors, actuators, and vibration control systems, see Bastola and Hossain [25] for a thorough review. However, the existing silicone elastomers or their composites are not biocompatible and are not suitable for meniscal implants. Thus, a bio-compactible and 3D printable silicone-based elastomer is always worthy of investigation.

The soft silicone-based elastomers, Ecoflex, and their composites are attractive in a number of applications such as skin-mountable strain sensors, wearable energy devices, and displays [26][27][28][29], by virtue of their mechanical properties. The excellent mechanical properties of Ecoflex make it a promising candidate material for human implants. However, biocompatible Ecoflex elastomer 3D printing for human implants has not been reported.

Combining the superior properties of silicone with the unmet needs of the meniscus market, we have developed a 3D silicone meniscus implant which encompasses the features of an ideal meniscal implant: (1) cytocompatible, (2) resistant to cyclic loading and mechanically similar to native meniscus, and (3) directly 3D printable. In our previous investigations [30][31], we presented the development of the in-house 3D printer, rheological properties of printing ink, and optimization of the printing process. The main focus of this study is to determine whether the purity, composition, structure, dimensions and mechanical properties of silicone implants are affected by the use of a custom-made in-house 3D printer based on an open source software and commercially available 3D printer.

In this study, we have used a phosphate buffer saline (PBS) absorption test, surface profilometry, X-ray photoelectron spectroscopy (XPS), Fourier transform infrared (FTIR) spectroscopy, thermo-gravimetric analysis (TGA), scanning electron microscopy (SEM), and differential scanning calorimetry (DSC) to effectively assess and compare material properties between molded and 3D printed silicone samples. SEM is used to assess the surface morphology of silicone samples and to investigate the relative changes in surface roughness [32]. FTIR is used for detection of chemical changes and surface hydroxylation in damaged samples. XPS is used to analyze elemental composition changes on the surface of the sample. TGA and DSC are used to analyze the thermal stability of silicone samples. American Society for Testing and Materials (ASTM) 575 compression testings [33] and cyclic loading up to 1000 cycles [34] are used to assess the mechanical stability and robustness of the silicone meniscus implants. The PBS absorption test [35], together with surface roughness measurements [36] is used to evaluate the degree of hydrophobicity of silicone samples [37]. The former measures the swelling content of the silicone sample, while the latter is a line-profiling method which produces a quantitative profile of the surface by using a high-resolution probe to detect changes in the surface topography. The degree of hydrophobicity is correlated to the affinity for attachment of the extracellular matrix and subsequent cell adhesion, proliferation and differentiation [33][38]. Despite using biocompatible silicone resin components A and B, the final 3D printed silicone implant should still be tested for biocompatibility. Cell viability and proliferation assays [39] with L929 fibroblasts are used to assess the cytocompatibility of silicone meniscus implants.

2. Results and Discussion

2.1. Light Microscope

The random, stellated arrangement of the molded silicone samples in surface view (Figure 2a) and in cross-sectional view (Figure 2c) of the molded silicone samples contrast greatly with the regular, striated, laminated layer-by-layer fibrial appearances of the 3DP silicone samples in surface views (Figure 2b) and cross-sectional views (Figure 2d). No obvious manufacturing defect, tears or color discoloration was observed. This difference in architectural arrangement has great implications for mechanical and functional properties of silicone implants and will be discussed in later sections.

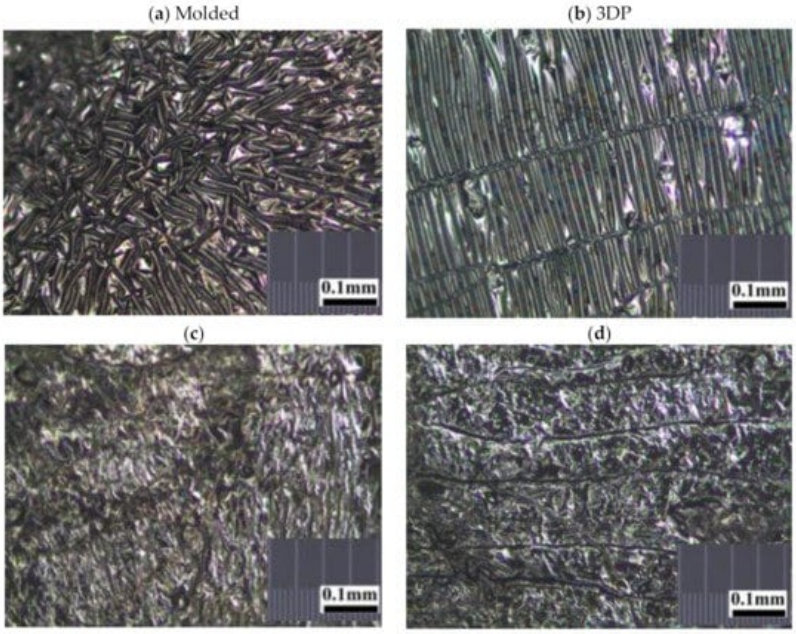

Figure 2. Representative stereomicroscopic images of the core surfaces of silicone meniscus implants. (**a**) surface of molded implant, (**b**) surface of 3D printed implant, (**c**) cross-section of molded implant and (**d**) cross-section of 3D printed implant (20× magnification).

2.2. Scanning Electron Microscopy

Images from SEM clearly demonstrated that different manufacturing methods led to distinct surface patterns of the silicone meniscus. Figure 3a,c,e depicted the irregular, smooth, and diffuse surface patterns on molded silicone implants, whereas Figure 3b,d,f portrayed the wavy, regular, mosaic surface patterns on 3D printed silicone implants. In both groups, SEM images did not reveal any fracture, tear, or heavy metal contamination.

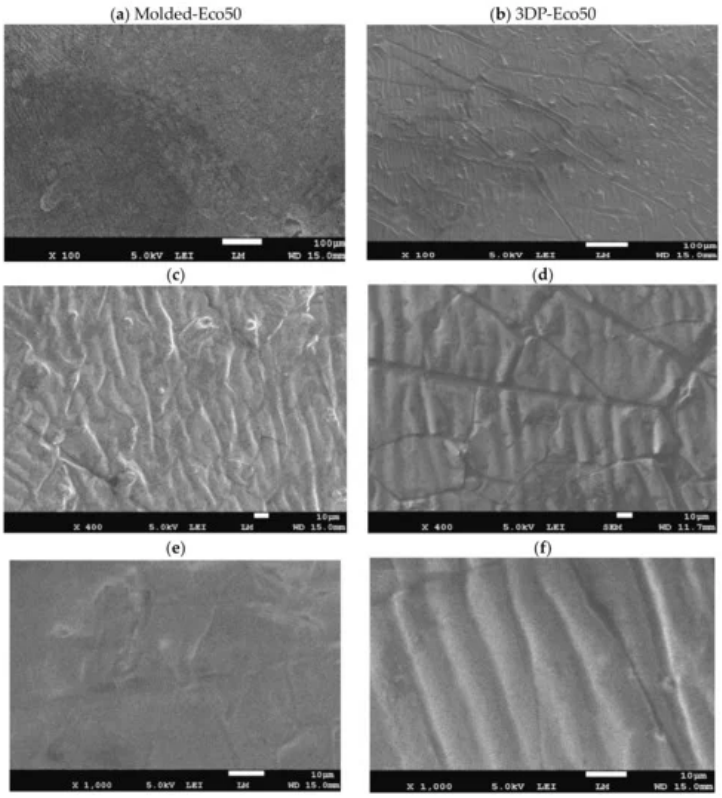

Figure 3. Representative scanning electron microscope (SEM) pictures (magnification 100×, 400× and 1000×) showing the different surface patterns of (**a**,**c**,**e**) molded silicone and (**b**,**d**,**f**) 3D-printed silicone.

2.3. PBS Absorption Test

The PBS absorption tests indicated that the water content of both Eco30 and Eco50 silicone meniscus did not show any significant change at pre-soak, 24 h post-soak and 120 h of post-soak (Figure 4). These results are in accordance with those of Bo Gong's study [35] which proved that water absorption by silicone rubber material obeyed Fick's law. As shown in Equation (1) below, Fick's law expresses moisture content c(t) as a function of the diffusion coefficient D and the maximum moisture content c_s in wt% at the absorption equilibrium. Based on the results, the maximum moisture content Cs was determined to be 0.36% for Eco30 meniscus implants and 0.47% for Eco50 meniscus implants. These values were slightly higher than the Cs value 0.23% in Bo Gong's study which assumed that diffusion only occurs from the top and bottom surfaces of their silicone samples. There is no statistically significant difference in water content pass the 24 h time point which clearly indicated that the water content have already stabilised within 24 h of the soaking period. Extrapolating from these results, the meniscus implant should also have attained its final size and shape within 24 h of arthroscopic insertion into the knee joint.

(1)

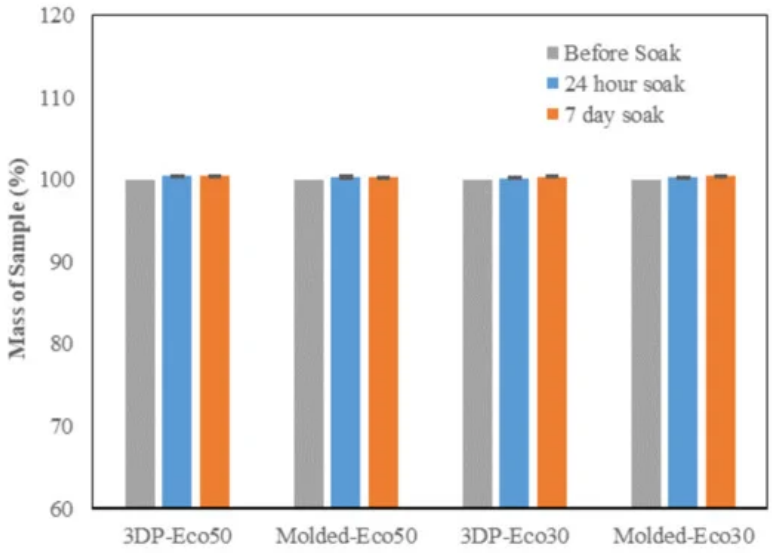

Figure 4. Phosphate buffer absorption test for silicone meniscus implants Ecoflex 50 and 30.

2.4. Surface Profilometry

This method uses a high-resolution probe to detect the surface topography in order to produce a quantitative profile of the surface. The surface of the anterior horn, body and posterior horns of the silicone meniscus were scanned in triplicates. The results from Figure 5 indicated that there is no statistically significant difference in surface roughness between both molded and 3D printed Eco30 and Eco50 silicone implants. However, this is likely due to limitations from the small sample size.

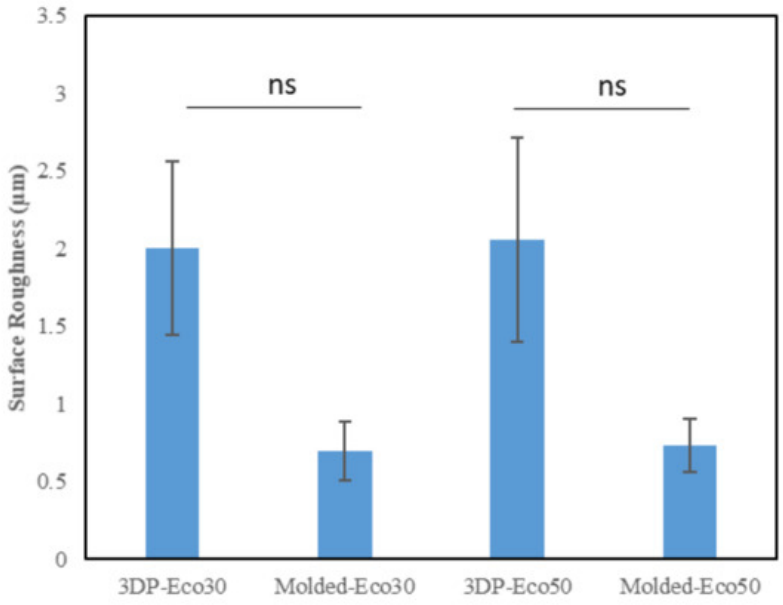

Figure 5. Surface roughness (µm) of the two silicone elastomers (Ecoflex-30 and Ecoflex-50) manufactured by molding and 3D printing.

2.5. X-ray Photoelectron Spectroscopy

The atomic composition and XPS spectra of molded and 3D printed silicone implant is shown below in Table 2 and in Supplementary Materials Figure S2, respectively. Both molded and 3D printed Eco50 silicone implants display similar silicone composition of 99.7% and 99.8%, respectively (element 14 Si, K alpha-1.740, K beta-1.829, Kab-1.84). The sulphur, iron and copper elements detected are quite possibly additives within the resins. No carbon-black fillers and heavy metal contamination was observed in both groups.

Table 2. Atomic Composition obtained for molded and 3D Printed Silicone Implant.

Samples	Si (%)	S (%)	Fe (%)	Cu (%)
Eco50 molded implant	**99.739**	**0.253**	**0.005**	**0.003**
Eco50 3D-printed implant	**99.816**	**0.174**	**0.005**	**0.01**

2.6. FTIR

FTIR was used to evaluate changes in molecular structure and functional groups of 3D printed and molded silicone samples. The FTIR results are depicted in Figure 6. The absorption peaks at 3000 cm^{-1} correspond to the stretching vibration of methyl (-CH_3). The weak absorption peak at 1400 cm^{-1} correspond to the asymmetric Si-CH3 stretching. The stronger absorption peaks at 1255 cm^{-1}, 1000–1100 cm^{-1}, and 800 cm^{-1} are attributed to Si-CH_3, Si-O-Si, and Si-$(CH_3)_2$ bonds, respsectively. All these peaks represent characteristic peaks of silicone rubber.

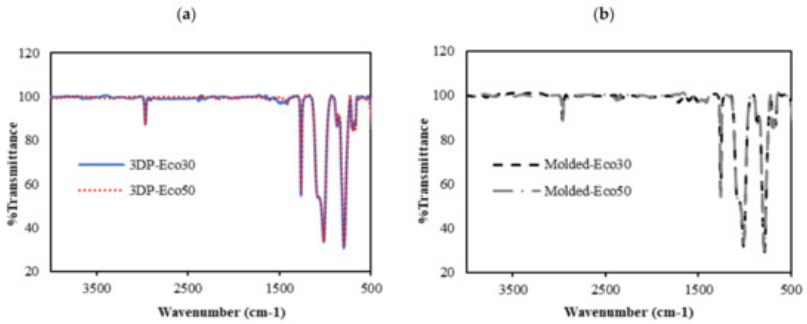

Figure 6. FTIR absorbance spectra of (**a**) 3D printed silicone implant and (**b**) molded silicone sample.

From Figure 6a,b, it can be observed that the FTIR spectra of both 3DP and molded Eco30 and Eco50 silicone samples show exactly the same peaks, indicating that the heat-curing processes (<120 °C) during 3D printing did not alter the chemical composition of the Ecoflex silicone. Also, the flow of silicone resins through the 3D printer did not cause any unwanted contamination of the resins.

2.7. DSC/TGA/DTG

TGA measures sample mass as a function of temperature or time and is frequently used in quality control or product development to identify the different components of elastomers such as moisture, solvents, polymers, plasticizers, carbon black or inorganic fillers.

The TGA analysis of Ecoflex silicone elastomer comprises of three steps (Figure 7). The DTG curve (the first derivative of the TGA curve) is used to determine the temperature limits for evaluation. The first step below ~300 °C amounts to 3.1% and corresponds to the loss of small quantities of relatively volatile un-crosslinked chemicals. Between 300 and 550 °C, pyrolysis of the silicone takes place. Polymer content was determined to be about 59.937% and 61.95% in the molded and 3D printed silicone sample, respectively (Table 3). The residual silica content was determined to be about 40.073% in the molded sample and 38.053% in the 3D printed sample. To oxidize the carbon black formed during pyrolysis, the atmosphere is switched from nitrogen to air at 600 °C. With many elastomers, the amount of carbon black formed during pyrolysis can be neglected. The carbon black filler content can therefore be determined from the third step between 600 and 700 °C and yields a value of 40.03% and 38.05% in molded and 3D printed silicone samples, respectively. The final residue comprised of inorganic fillers such as silicates of oxides. The first derivative of the TGA curve is represented by the DTG curve and can be used to quantify the decomposition rate.

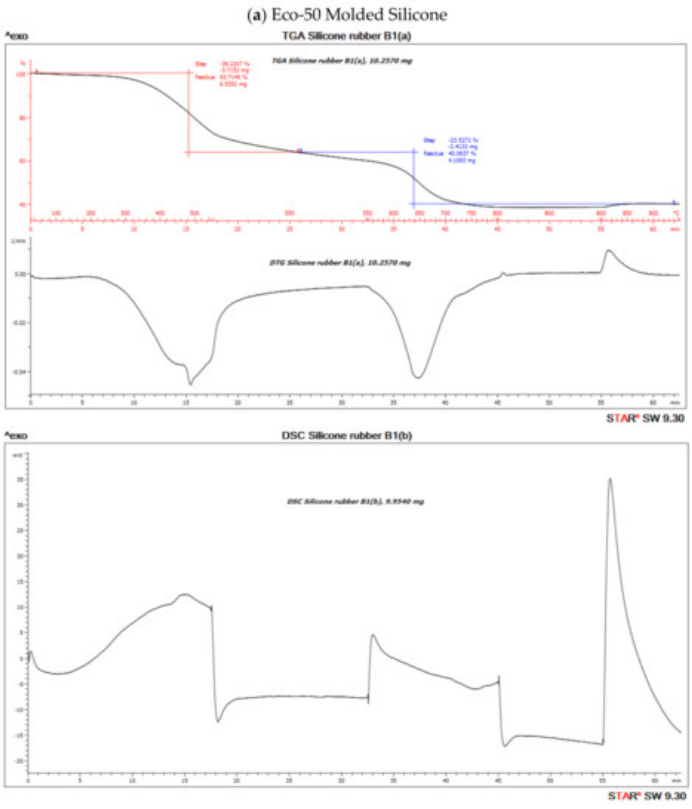

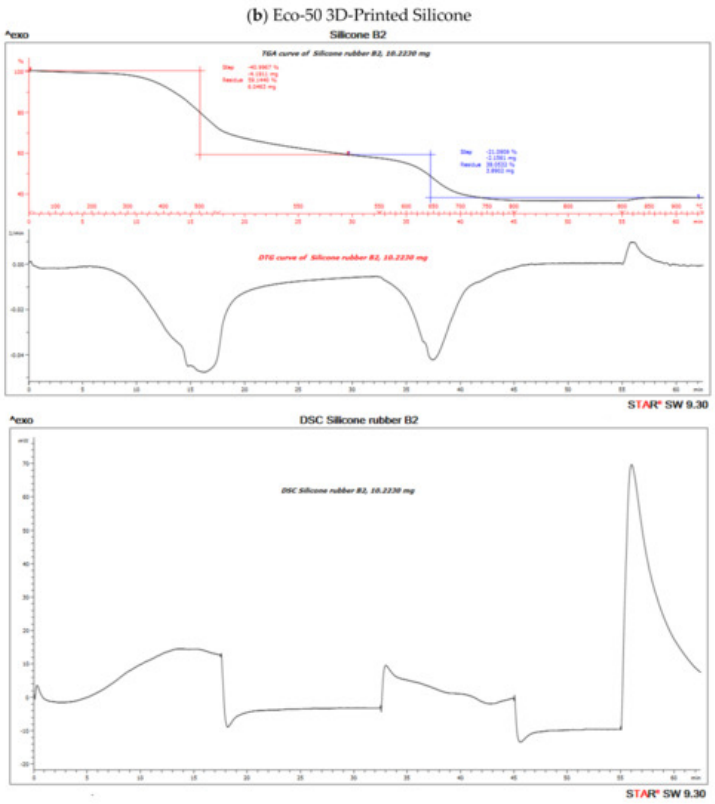

Figure 10. Thermo-gravimetric analysis/differential scanning calorimentry (TGA/DSC) curves of (**a**) molded and (**b**) 3D-Printed silicone Ecoflex 50 measured from 30 to 700 °C at a heat rate of 20 K/min. The TGA curve (red) measures the loss of mass and the DSC curve (black) provides information about endothermic and exothermic effects.

Table 3. Percentage (%) polymer content of material and % residual silicates/oxides.

Samples	% Polymer Content	% Residual Silicates/Oxides
Eco-50 Molded Silicone implant	**59.937**	**40.073**
Eco-50 3D Printed Silicone implant	**61.95**	**38.053**

Both molded and 3D printed methods of Eco50 silicon samples show similar percentages of thermal degradation of silicone (Supplementary Materials Figure S3). At any heating temperatures, more heat inflow is required for Eco50 samples to attain the same temperature, when compared to Eco30 samples, as shown in Supplementary Materials Figure S3a. The results also prove that 3D printed silicone samples will remain thermally stable for heat sterilization processes, such as autoclaving at 121 °C, exhibiting no significant loss of mass for temperatures up to 300 °C.

2.8. Cytocompatibility of Molded and 3D-Printed Silicone

Implantation of biomaterials could cause host reactions such as blood-material interactions, tissue injury, foreign body reaction, inflammation, and fibrosis/fibrous capsule development. In the very early process of implantation, blood/material interactions occur with protein adsorption to the biomaterial surface and development of a blood-based transient provisional matrix that forms on and around the biomaterial.

In order to investigate the extent of foreign body reaction, L929 fibroblasts were seeded and allowed to proliferate in culture medium on molded or 3D-printed silicone samples for 24, 72, and 120 h. The silicone samples were already subject to sterilization with ethanol and UV-C irradiation before use in our studies and did not exhibit any significant changes in properties. After washing steps, the cells were re-seeded to study cell adhesion to silicone samples. The results from Figure 8b demonstrated that cells remained spherical and did not form an extended morphology typical of attached cells in a 2D culture (Supplementary Materials Figure S4). The results indicate that fibrosis/fibrous capsule development does not take place even when fibroblasts were in direct contact with silicone surface up to 120 h. However, the re-seeded fibroblasts continued to show contact-inhibited growth for up to 120 h and started to form cell clusters on the surface due to the low cytotoxicity of the silicone samples (Figure 8a). Furthermore, it appears that a correlation exists between surface roughness and contact-inhibited growth of cells on silicone surface. This could be attributed to more cells physically anchoring themselves to the surface of 3D printed silicone by virtue of the increased surface roughness as shown in Figure 5.

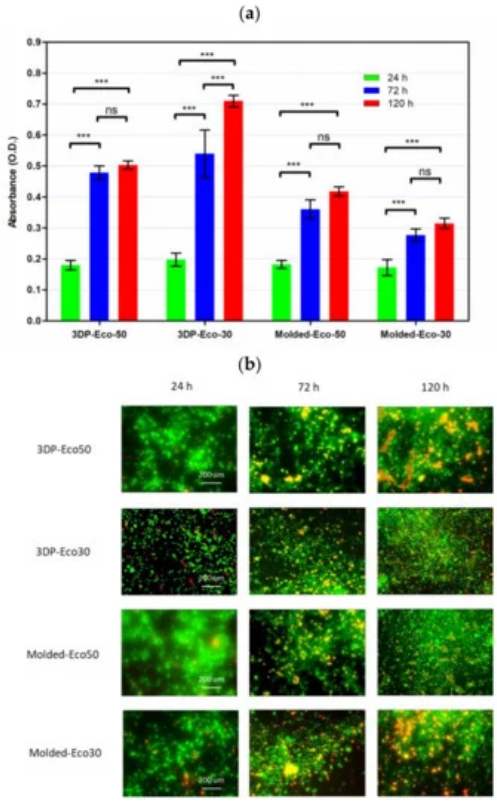

Figure 8. (**a**) Cell proliferation of re-seeded L929 cells on printed/casted Eco50/Eco30 substrates after 24, 72, and 120 h culture was quantified based on the WST-8 cell proliferation assay. (**b**) Fluorescent images of re-seeded L929 cells on printed/casted Eco50/Eco30 substrates after 24, 72, and 120 h culture. Cells were stained with the Live/Dead® cell viability assay. Statistical significance between groups was assessed using two-way analysis of variance (ANOVA) followed by Bonferroni post-tests. ns = $p > 0.05$ and *** = $p < 0.001$.

2.9. Mechanical Compression Test

The overall non-linear stress-strain responses of both Ecoflex30 and Ecoflex50 silicone elastomers under monotonic compressive loading up to failure showed linear elastic region at low strain level and followed by a non-linear region at higher strain level before failure.

Cyclic loading at 4-cycles for Eco30 and Eco50 silicones are shown in Figure 9. The graphs also showed hysteresis and strain hardening, which are viscoelastic properties of silicone. The initial compressive modulus at the linear region is the functioning modulus of the meniscus implant. It can be estimated from the slope of the curve in the 10% to 30% strain range. In hysteresis, the loop area enclosed by the loading and unloading pathways represents the energy loss in the system. This area is more pronounced at higher strain rates and with Eco50 silicone resins, indicating more mechanical damping in the system due to higher viscosity. However, the hysteresis effect decreases with an increasing number of cycles of cyclic loading.

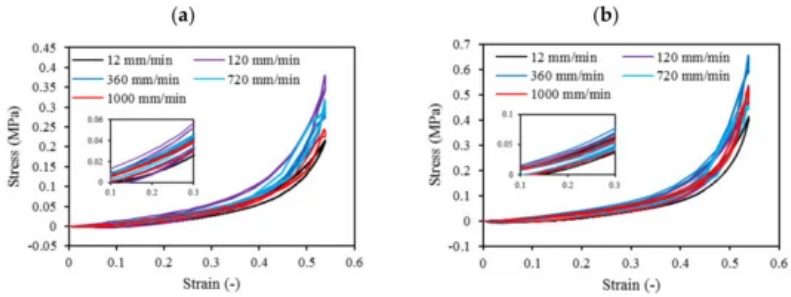

Figure 9. Four-cycle cyclic stress-strain for (**a**) STD-Eco30 and (**b**) STD-Eco50 at strain rates of 12, 120, 360, 720, and 1000 mm/min.

Mechanical properties of soft polymers in cyclic loading is one of the important material properties to be understood for their successful implementation in the actual system for the long run. Usually, Ecoflex of higher Shore hardness exhibits greater stiffness and larger hysteresis. The viscoelastic behavior of Ecoflex silicone elastomers has been extensively

investigated by Liao et al. [40][41]. In their experiments, tensile properties and hysteresis of Ecoflex elastomers with different hardness have been reported. Our cyclic test results in a compression mode are highly coherent to Liao et al. [40] [41] cyclic test results in a tensile mode.

Strain hardening is the strengthening of material properties with repeated elastic deformation. This phenomenon is observed in both Eco30 and Eco50 silicone implants. Strain hardening is observed especially at low strain rates up to 200 mm/min before stabilizing at higher strain rates at 800 mm/min. A less viscous sample takes more cycles for strain hardening effect to stabilize [34].

At all values of strain rates, Eco50 silicone implants consistently demonstrated higher compressive modulus and stress values than their Eco30 counterparts. At cyclic loading of 1000-cycles, Eco50 meniscus implants also demonstrated higher stress at failures, when compared to their Eco30 meniscus implant counterparts (Figure 10 and Figure 11). In Figure 8, the red line represents the 4-cycle run at a strain rate of 1000 mm/min and is almost a straight line when tested to a strain of 0.3, after which a curvilinear line is observed up to a strain of 0.5. Lines of other colors represent 4-cycle run at other strain rates. Figure 10 and Figure 11 showed 1000 overlapping lines after a run of 1000-cycle at 1000 mm/min. In the first four cycle runs, similar trends were observed as in Figure 9. Subsequent lines with steeper gradients showed strain hardening characteristics. Comparing Figure 9, Figure 10 and Figure 11 at the same strain rate of 1000 mm/min, similar trends were observed, ie linear up to a strain of 0.3 and curvilinear from strain of 0.3 to 0.5. The modulus of Eco30 and Eco50 samples are 0.161, 0.219, 0.202, 0.179, and 0.174 MPa and 0.247, 0.304, 0.304, 0.246, and 0.241 MPa, respectively, at a strain rate of 12, 120, 360, 720, and 1000 mm/min (Figure 12).

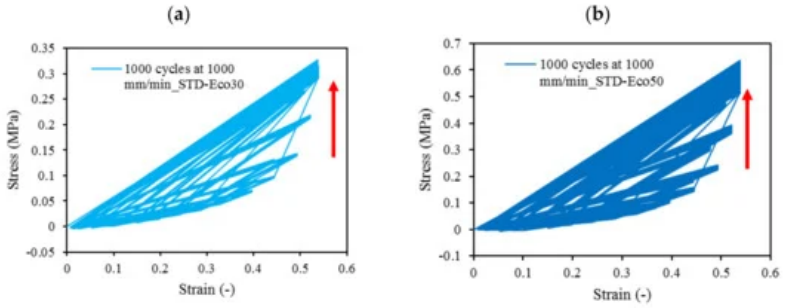

Figure 10. 1000-cycle cyclic stress-strain for (**a**) STD-Eco30 and (**b**) STD-Eco50, at a strain rate of 1000 mm/min.

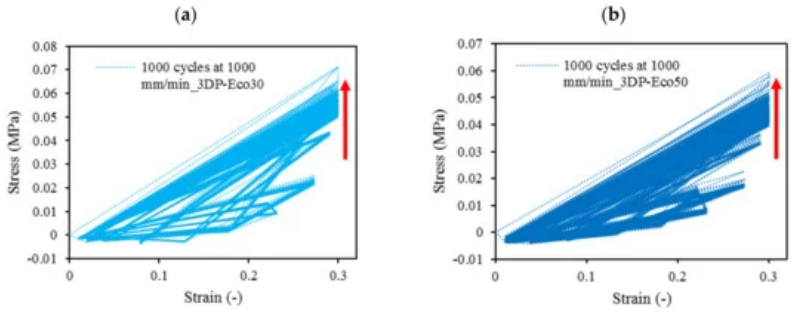

Figure 11. The 1000-cycle cyclic stress-strain for (**a**) 3DP-Eco30 and (**b**) 3DP-Eco50, at a strain rate of 1000 mm/min.

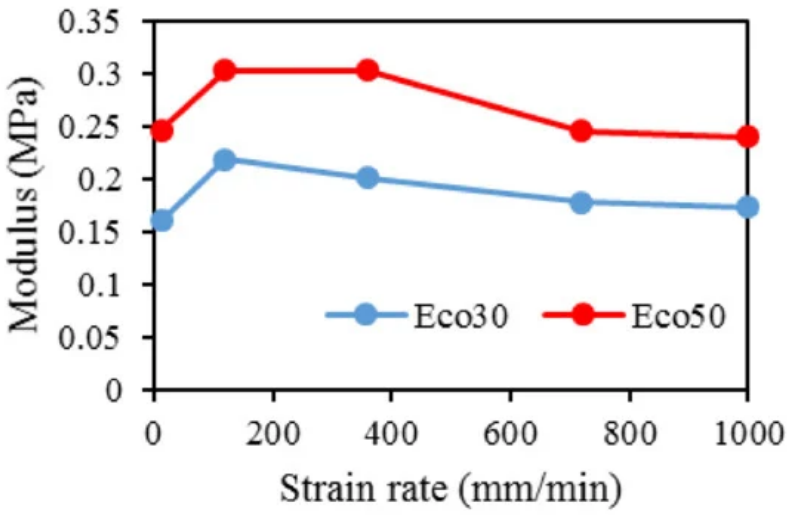

Figure 12. Modulus for Eco30 and Eco50 at different strain rates.

3. Conclusions

This study concludes that the silicone 3D printing process does not permanently change the overall physical, biochemical, or mechanical properties of the 3D printed silicone meniscus. There was no statistically significant difference in surface roughness properties and water absorption characteristics between molded and 3D Printed samples of Eco30 and Eco50. There is no shelf life for these 3D printed models. Results from FTIR and TGA/DSC demonstrated the chemical and thermal stabilities of Ecoflex silicone rubber, respectively. Both Eco30 and Eco50 demonstrated viscoelastic properties of strain hardening and hysteresis. At all strain rates, Eco50 silicone meniscus implants and standard samples consistently displayed higher stiffness and modulus as compared to Eco30 samples. Finally, cytotoxicity tests proved that both Eco30 and Eco50 silicone implants are biocompatible.

References

1. Shane Anderson, A.; Loeser, R.F. Why is osteoarthritis an age-related disease? Best Pract. Res. Clin. Rheumatol. 2010, 24, 15–26.
2. Loeser, R.F. Age-related changes in the musculoskeletal system and the development of osteoarthritis. Clin. Geriatr. Med. 2010, 26, 371–386.
3. Jonathan, E.; Vincenzo, C.; Claudio, Z.; Peter, V.; Ron, A.; Elliott, H.; Farshid, G.; Avi, S.; Eran, L.-G.; Emanuele, N. A novel polycarbonate-urethane meniscal implant: From bench to first clinical experience. Orthop. Proc. 2012, 94-B, 125.
4. Bulgheroni, P.; Murena, L.; Ratti, C.; Bulgheroni, E.; Ronga, M.; Cherubino, P. Follow-up of collagen meniscus implant patients: Clinical, radiological, and magnetic resonance imaging results at 5 years. Knee 2010, 17, 224–229.
5. Bouyarmane, H.; Beaufils, P.; Pujol, N.; Bellemans, J.; Roberts, S.; Spalding, T.; Zaffagnini, S.; Marcacci, M.; Verdonk, P.; Womack, M.; et al. Polyurethane scaffold in lateral meniscus segmental defects: Clinical outcomes at 24 months follow-up. Orthop. Traumatol. Surg. Res. 2014, 100, 153–157.
6. Baynat, C.; Andro, C.; Vincent, J.P.; Schiele, P.; Buisson, P.; Dubrana, F.; Gunepin, F.X. Actifit® synthetic meniscal substitute: Experience with 18 patients in Brest, France. Orthop. Traumatol. Surg. Res. 2014, 100, S385–S389.
7. Liravi, F.; Toyserkani, E. A hybrid additive manufacturing method for the fabrication of silicone bio-structures: 3D printing optimization and surface characterization. Mater. Des. 2018, 138, 46–61.
8. Grogan, S.P.; Chung, P.H.; Soman, P.; Chen, P.; Lotz, M.K.; Chen, S.; D'Lima, D.D. Digital micromirror device projection printing system for meniscus tissue engineering. Acta Biomater. 2013, 9, 7218–7226.
9. Kobayashi, M.; Toguchida, J.; Oka, M. Development of an artificial meniscus using polyvinyl alcohol-hydrogel for early return to, and continuance of, athletic life in sportspersons with severe meniscus injury. I: Mechanical evaluation. Knee 2003, 10, 47–51.
10. Kelly, B.T.; Robertson, W.; Potter, H.G.; Deng, X.-H.; Turner, A.S.; Lyman, S.; Warren, R.F.; Rodeo, S.A. Hydrogel meniscal replacement in the sheep knee: Preliminary evaluation of chondroprotective effects. Am. J. Sports Med. 2007, 35, 43–52.
11. Karstedt, B. Platinum Complexes of Unsaturated Siloxanes and Platinum Containing Organopolysiloxanes. U.S. Patent 3,775,452, 27 November 1973.
12. Kim, Y.; Yuk, H.; Zhao, R.; Chester, S.A.; Zhao, X. Printing ferromagnetic domains for untethered fast-transforming soft materials. Nature 2018, 558, 274–279.
13. Bastola, A.K.; Paudel, M.; Li, L. Development of hybrid magnetorheological elastomers by 3D printing. Polymer 2018, 149, 213–228.
14. O'Bryan, C.S.; Bhattacharjee, T.; Hart, S.; Kabb, C.P.; Schulze, K.D.; Chilakala, I.; Sumerlin, B.S.; Sawyer, W.G.; Angelini, T.E. Self-assembled micro-organogels for 3D printing silicone structures. Sci. Adv. 2017, 3, e1602800.
15. Yuk, H.; Zhao, X. A New 3D printing strategy by harnessing deformation, instability, and fracture of viscoelastic inks. Adv. Mater. 2018, 30, 1704028.
16. Bastola, A.K.; Hoang, V.T.; Li, L. A novel hybrid magnetorheological elastomer developed by 3D printing. Mater. Des. 2017, 114, 391–397.
17. Bezek, L.B.; Cauchi, M.P.; De Vita, R.; Foerst, J.R.; Williams, C.B. 3D printing tissue-mimicking materials for realistic transseptal puncture models. J. Mech. Behav. Biomed. Mater. 2020, 110, 103971.

18. Hossain, M.; Liao, Z. An additively manufactured silicone polymer: Thermo-viscoelastic experimental study and computational modelling. Addit. Manuf. 2020, 35, 101395.
19. Zhao, T.; Yu, R.; Li, S.; Li, X.; Zhang, Y.; Yang, X.; Zhao, X.; Wang, C.; Liu, Z.; Dou, R.; et al. Superstretchable and processable silicone elastomers by digital light processing 3D printing. ACS Appl. Mater. Interfaces 2019, 11, 14391–14398.
20. McCoul, D.; Rosset, S.; Schlatter, S.; Shea, H. Inkjet 3D printing of UV and thermal cure silicone elastomers for dielectric elastomer actuators. Smart Mater. Struct. 2017, 26, 125022.
21. Davoodi, E.; Fayazfar, H.; Liravi, F.; Jabari, E.; Toyserkani, E. Drop-on-demand high-speed 3D printing of flexible milled carbon fiber/silicone composite sensors for wearable biomonitoring devices. Addit. Manuf. 2020, 32, 101016.
22. Zhou, L.-y.; Gao, Q.; Fu, J.-z.; Chen, Q.-y.; Zhu, J.-p.; Sun, Y.; He, Y. Multimaterial 3D Printing of Highly Stretchable Silicone Elastomers. ACS Appl. Mater. Interfaces 2019, 11, 23573–23583.
23. Abdollahi, S.; Markvicka, E.J.; Majidi, C.; Feinberg, A.W. 3D printing silicone elastomer for patient-specific wearable pulse oximeter. Adv. Healthc. Mater. 2020, 9, 1901735.
24. Menon, A.; Póczos, B.; Feinberg, A.W.; Washburn, N.R. Optimization of silicone 3D printing with hierarchical machine learning. 3D Print. Addit. Manuf. 2019, 6, 181–189.
25. Bastola, A.K.; Hossain, M. A review on magneto-mechanical characterizations of magnetorheological elastomers. Compos. Part B Eng. 2020, 200, 108348.
26. Amjadi, M.; Yoon, Y.J.; Park, I. Ultra-stretchable and skin-mountable strain sensors using carbon nanotubes–Ecoflex nanocomposites. Nanotechnology 2015, 26, 375501.
27. Siegenthaler, K.; Künkel, A.; Skupin, G.; Yamamoto, M. Ecoflex® and Ecovio®: Biodegradable, performance-enabling plastics. In Synthetic Biodegradable Polymers; Rieger, B., Künkel, A., Coates, G., Reichardt, R., Dinjus, E., Zevaco, T., Eds.; Springer: Berlin/Heidelberg, Germany, 2011; Volume 245, pp. 91–136.
28. Mai, H.; Mutlu, R.; Tawk, C.; Alici, G.; Sencadas, V. Ultra-stretchable MWCNT-Ecoflex piezoresistive sensors for human motion detection applications. Compos. Sci. Technol. 2019, 173, 118–124.
29. Xu, Z.; Zheng, S.; Wu, X.; Liu, Z.; Bao, R.; Yang, W.; Yang, M. High actuated performance MWCNT/Ecoflex dielectric elastomer actuators based on layer-by-layer structure. Compos. Part A Appl. Sci. Manuf. 2019, 125, 105527.
30. Luis, E.; Pan, H.M.; Sing, S.L.; Bajpai, R.; Song, J.; Yeong, W.Y. 3D direct printing of silicone meniscus implant using a novel heat-cured extrusion-based printer. Polymers 2020, 12, 1031.
31. Luis, E.; Pan, H.M.; Sing, S.L.; Bastola, A.K.; Goh, G.D.; Goh, G.L.; Tan, H.K.J.; Bajpai, R.; Song, J.; Yeong, W.Y. Silicone 3D printing: Process optimization, product biocompatibility, and reliability of silicone meniscus implants. 3D Print. Addit. Manuf. 2019, 6, 319–332.
32. Setua, D.; Awasthi, R.; Kumar, S.; Prasad, M.; Agarwal, K. Scanning electron microscopy of natural rubber surfaces: Quantitative statistical and spectral texture analysis using digital image processing. In Microscopy: Science Technology Application and Education; Formatex Research Center: Badajos, Spain, 2018.
33. Heinrichs, V.; Dieluweit, S.; Stellbrink, J.; Pyckhout-Hintzen, W.; Hersch, N.; Richter, D.; Merkel, R. Chemically defined, ultrasoft PDMS elastomers with selectable elasticity for mechanobiology. PLoS ONE 2018, 13, e0195180.
34. Lee, W.S.; Yeo, K.S.; Andriyana, A.; Shee, Y.G.; Mahamd Adikan, F.R. Effect of cyclic compression and curing agent concentration on the stabilization of mechanical properties of PDMS elastomer. Mater. Des. 2016, 96, 470–475.
35. Gong, B.; Tu, Y.; Zhou, Y.; Li, R.; Zhang, F.; Xu, Z.; Liang, D. Moisture absorption characteristics of silicone rubber and its effect on dielectric properties. In 2013 Annual Report Conference on Electrical Insulation and Dielectric Phenomena, Proceedings of the Conference on Electrical Insulation and Dielectric Phenomena (CEIDP), Shenzhen, China, 20–23 October 2013; IEEE: New York, NY, USA, 2013; pp. 430–433.
36. Vorburger, T.V.; Rhee, H.-G.; Renegar, T.B.; Song, J.-F.; Zheng, A. Comparison of optical and stylus methods for measurement of surface texture. Int. J. Adv. Manuf. Technol. 2007, 33, 110–118.
37. Tokoro, T. Effects of temperature and surface roughness on the evaluation of hydrophobic properties of silicone rubber. In Proceedings of the IEEE Conference on Electrical Insulation and Dielectric Phenomena (CEIDP), Toronto, ON, Canada, 16–19 October 2016; pp. 814–817.
38. Campeau, M.-A.; Lortie, A.; Tremblay, P.; Béliveau, M.-O.; Dubé, D.; Langelier, È.; Rouleau, L. Effect of manufacturing and experimental conditions on the mechanical and surface properties of silicone elastomer scaffolds used in endothelial mechanobiological studies. Biomed. Eng. Online 2017, 16, 1–23.
39. Li, W.; Zhou, J.; Xu, Y. Study of the in vitro cytotoxicity testing of medical devices. Biomed. Rep. 2015, 3, 617–620.

40. Liao, Z.; Hossain, M.; Yao, X. Ecoflex polymer of different Shore hardnesses: Experimental investigations and constitutive modelling. Mech. Mater. 2020, 144, 103366.
41. Liao, Z.; Hossain, M.; Yao, X.; Navaratne, R.; Chagnon, G. A comprehensive thermo-viscoelastic experimental investigation of Ecoflex polymer. Polym. Test. 2020, 86, 106478.